Polyamide reverse osmosis membrane compaction and relaxation: Mechanisms and implications for desalination performance

Jishan Wu [a,1], Jinlong He [b,1], Javier A. Quezada-Renteria [a], Jason Le [c], Kay Au [c], Kevin Guo [c], Minhao Xiao [a], Xinyi Wang [a], Derrick Dlamini [a], Hanqing Fan [d], Kevin Pataroque [d], Yara Suleiman [e], Sina Shahbazmohamadi [e], Menachem Elimelech [d], Ying Li [b,**], Eric M. V. Hoek [a,f,*]

[a] Department of Civil & Environmental Engineering, University of California, Los Angeles, CA, 90095, USA
[b] Department of Mechanical Engineering, University of Wisconsin-Madison, Madison, WI, 53706, USA
[c] Department of Chemical & Biomolecular Engineering, University of California, Los Angeles, CA, 90095, USA
[d] Department of Chemical & Environmental Engineering, Yale University, New Haven, CT, 06511, USA
[e] Department of Biomedical Engineering, University of Connecticut, Storrs, CT, 06030, USA
[f] Energy Storage & Distributed Resources Division, Lawrence Berkeley National Lab, Berkeley, CA, 94720, USA

ARTICLE INFO

ABSTRACT

This work investigates the compaction and relaxation behavior of composite reverse osmosis (RO) polyamide (PA) selective layers, utilizing non-equilibrium molecular dynamic (NEMD) simulations and well-controlled permeation experiments. Composite PA-RO membranes are prepared by interfacial polymerization of para and meta diamine monomer blends to achieve different PA film crosslinking degrees (*CD*). Wet-testing results suggest that "tighter" (higher *CD*) composite RO membranes undergo 65 % less compaction and recover 17 % more of their initial permeability (termed "relaxation") when the pressure is relieved compared to lower *CD* PA layers. NEMD simulations provide a visual and quantitative characterization of PA layer's free volume changes *in operando*. NEMD simulations also corroborate experimental findings and elucidate the viscoelastic properties of the PA layer that govern compaction and relaxation behavior. The mechanisms of compaction under water permeation derived from NEMD simulations further support the notion of viscous flow of water through inter-connected free volume elements (i.e., "pores") within crosslinked PA films.

1. Introduction

Reverse osmosis (RO) is the most widely used and versatile water treatment technology available due to its ability to cost-effectively extract clean, fresh water from nearly any source water [1–3]. To date, most commercially available RO membranes comprise a tri-layer composite structure, prepared by polymerizing an ultra-thin, microporous polyamide (PA) coating film directly on top of a mesoporous polysulfone (PSF) support membrane previously phase inverted over a macroporous polyester (PET) nonwoven fabric. The PA coating is synthesized via an *in situ* polycondensation reaction between multi-functional amine and acid chloride monomers; the combination of *m*-phenylenediamine (MPD) and trimesoyl chloride (TMC) is frequently

used. Modern PA-PSF-PET tri-layer composite RO membranes excel in desalination and advanced water treatment due to their excellent water permeability and salt rejection as well as their chemical, mechanical, and thermal stability for traditional applications such as seawater desalination, brackish groundwater desalination, ultra-pure water production, and municipal water recycling. However, membrane fouling, scaling, and compaction remain challenges [4,5] with the latter being the focus herein.

Upon applying nearly any flux-generating feed pressure, the water permeability of the polymeric thin film composite (TFC) RO membranes quickly declines even when filtering ultra-pure, 18 MΩ deionized water. Notably, decreases of over 50 % have been reported at high applied pressures [4]. This performance loss is most often attributed to

compaction (or densification) of the mesoporous PSF support layer of the TFC membrane and has been confirmed by multiple studies [4,6,7]. Pendergast et al. [6] studied hand-cast composite RO membrane compaction at pressures up to 35 bar, observing a reduction in thickness of the PSF support layer of 20 %–30 % with up to 50 % loss of water permeability. Davenport et al. [7] observed a 35 % decrease in permeability and a 60 % reduction in cross-sectional thickness of commercial seawater RO membranes operated at 150 bar. More recently, Wu et al. [4] investigated commercial RO membrane compaction at pressures up to 207 bar, revealing that a 38 %–60 % thickness reduction in the PSF support layer contributed to over 50 % water permeability loss [4]. Densification of support membrane skin layer pores — located immediately underneath the PA coating film — increases the effective diffusion path length through the composite PA-PSF membrane structure, reducing the permeability of both salt and water [6].

While it is clear the mesoporous PSF support layer of the TFC membrane compacts and the composite RO membrane loses permeability, some uncertainty remains about the possible role of compaction in the ultra-thin, dense PA coating film of the TFC. In one recent study, transmission electron microscopy (TEM) and atomic force microscopy (AFM) suggest there was no irreversible compaction of a PA selective layer compaction — the thickness and roughness of the PA film before and after pressurized testing were statistically identical [7]. In contrast, Chu et al. [8] reported significant PA layer compaction by measuring PA free volume and thickness reduction using positron annihilation lifetime spectroscopy (PALS), time-of-flight secondary ion mass spectrometry (ToF-SIMS), and stylus profilometry. All characterization methods for the PA coating film — including SEM, TEM, AFM, PALS, ToF-SIMS, and stylus profilometry — compared pristine and compacted RO membrane after the pressure was released. After the removal of applied pressure, the crosslinked PA layer may relax such that the effects of compaction are, at least partially, reversible. This is called membrane "relaxation" [9]. Membrane relaxation may occur to varying extents for wet and dry membranes, and over time; hence, changes to the membrane morphology could be different for different membrane handling and sample preparation procedures. *In situ* characterization methods could possibly enhance our understanding of PA selective layer compaction and relaxation behavior, but such techniques are not readily available to date.

Molecular dynamics (MD) simulations offer unique opportunities to visualize and quantify molecular scale phenomena, and to connect molecular interactions to macroscopic performance properties [10]. MD simulations have been applied in RO membrane research to gain insights into membrane synthesis [11–13], manufacturing [12], and transport [14]. Recently, Wang et al. [14] discussed the water transport mechanism through the PA film using non-equilibrium MD (NEMD) simulations, aided with permeation experiments. They concluded that water transport in the PA selective layer occurs via viscous flow through interconnected free volume elements or "pores" driven by a pressure gradient [15]. Although MD simulations are computationally intensive, they can be effective for gaining a better understanding of *in situ* and *in operando* membrane behavior (at the molecular scale), which cannot be achieved via *ex situ* (after the fact) experimental characterizations.

Herein, we combine controlled permeation experiments with NEMD simulations to shed new light on the mechanisms of PA layer film compaction and relaxation. We prepared five different composite RO membranes on identical substrates with varying crosslinking-degree (*CD*) in the PA film by tailoring the mole ratio of MPD and *p*-phenylenediamine (PPD) monomers during interfacial polymerization. RO permeation experiments aided with MD simulations confirm that composite PA-RO membranes with a higher *CD* exhibit lower water permeability, higher salt rejection, less compaction, and greater recovery of permeability via relaxation.

2. Materials and methods

2.1. Materials

A commercial, mesoporous PSF support membrane was used in all hand-cast membranes (PS20, Solecta, Inc., Oceanside, CA). Commercial RO membranes were also used for comparison with hand-cast membranes (FilmTec SW30XFR and BW30XFRLE, DWS Advantage, Bellevue, Washington, USA). Hexane, TMC 98 %, MPD flakes >99 %, PPD flakes >99 %, PEG, (+)-Camphor-10-sulfonic acid (CSA), triethylamine (TEA), and citric acid were purchased from Sigma Aldrich (St. Louis, Missouri, USA). IsoparG was procured from Gallade Chemical Inc. (Santa Ana, CA, USA). Different blends of MPD and PPD in 18 MΩ de-ionized (DI) water were reacted with TMC in hexane/isoparG to form the PA coating films via interfacial polymerization.

2.2. Membrane preparation

Five distinct composite RO membranes were prepared by interfacial polymerization of different monomer combinations. These membranes were synthesized with the same commercial PSF support membrane, but with different PA selective layers. The membrane performance, compaction and relaxation differences should be attributable solely to differences in the PA coating films. To alter the crosslinking-degree, as well as the microstructure of the PA selective layer, three sets of amine monomer solutions were used to prepare five different RO membranes as shown in Table S2. Detailed description of the membrane preparation and all following experimental approaches can be found in the supplementary information.

2.3. Membrane wet-testing

Water flux and salt rejection measurements were made using a rapidly stirred, dead-end filtration cell (HP4750X Hastelloy Stirred Cell, Sterlitech Corp) at 60 bar applied pressure. The schematic of the experimental filtration apparatus can be found in previous work [4].

For relaxation experiments, the pressure was released and then reapplied for further flux and rejection measurements. A single 30-min relaxation time was employed for the wet-testing of hand-cast membranes because no significant difference was observed for the commercial RO membrane beyond 30-min relaxation timeFig. S1.

In salt rejection experiments, 32 g/L of NaCl (Sigma Aldrich, S7653) were prepared in DI water as the feed solution. The osmotic pressure of the feed solution was calculated via the following polynomial fit to data produced by a commercial geochemical modeling software (OLI Systems, Inc. Parsippany, NJ, USA):

$$\pi = 0.741829c + 0.00111004c^2 \tag{1}$$

where π is the osmotic pressure (bar), and c denotes salt concentration in g-NaCl/L-H$_2$O.

Water flux J_w and salt flux J_s are determined from [16].

$$J_w = A(\Delta p_m - \Delta \pi_m) \tag{2}$$

$$J_s = B\Delta c_m. \tag{3}$$

Here A indicates the observed water permeance of the membrane, Δp_m is the *trans*-membrane hydraulic pressure, $\Delta \pi_m$ is the osmotic pressure difference across the membrane, B is the NaCl permeance of the membrane, and Δc_m is the real concentration difference across the membrane.

The concentration polarization factor (CP) is calculated according to [2,17–19].

$$CP = \frac{c_m}{c_b} = 1 - R_{ob} + R_{ob} \exp\left(\frac{J_w}{k_s}\right) \tag{4}$$

where R_{ob} ($=1-c_p/c_f$) is the observed salt rejection, k_s is the solute mass transfer coefficient, c_m is the membrane surface salt concentration, c_p is the permeate salt concentration, and c_f the (bulk) feed salt concentration. For the turbulent flow in a stirred-cell (Re > 32,000), the mass transfer coefficient is related to the Sherwood number [16], Sh, according to

$$k_s = Sh \frac{D}{d} \tag{5}$$

$$Sh = 0.04\, Re^{0.75} \bullet Sc^{0.33}, \text{and} \tag{6}$$

$$Re = \frac{d^2 \bullet \omega \bullet \rho}{\mu} \tag{7}$$

Here D is the diffusion coefficient, d the diameter of the stir cell, Re the Reynolds number, ω the rotation speed revolutions per second, ρ the liquid mass density, μ the dynamic viscosity and Sc the Schmidt number ($=\nu/D$), where ν is the kinetic viscosity ($=\mu/\rho$). The intrinsic rejection r_s and salt permeance can be determined by

$$r_s = 1 - \frac{C_p}{C_f \bullet CP} \tag{8}$$

$$B = \frac{J_w(1 - r_s)}{r_s} \tag{9}$$

Also, since the permeance, A, value of an RO membrane changes with the concentration of salt in the feedwater to which it is exposed [20], the A value in the presence of salt water can be determined from eq (2) where

$$\Delta\pi_m = \left(CP \bullet c_f - c_p\right). \tag{10}$$

The relaxation ratio (RR) in the wet testing is determined by

$$RR = \frac{A_{90} - A_{60}}{A_0} \tag{11}$$

where A_t stands for the water permeance at time t. The choice of 60 and 90 min, is informed by preliminary data shown in Fig. S1, which indicated that a 30-min relaxation interval is sufficient for the membrane to recover from reversible compaction. Similarly, the extent of compaction (XC) is defined as

$$XC = \frac{A_0 - A_t}{A_0}. \tag{12}$$

2.4. Composite membrane physical-chemical characterization

Membrane samples were characterized via scanning electron microscopy (SEM) using standard procedures [21] (Zeiss Supra 40 VP, Carl Zeiss Microscopy, LLC, NY). SEM images were of sufficiently high quality to enable estimation of PA selective layer thickness using software, Phenom image viewer (Thermo Fisher Scientific Inc., Waltham, MA, USA). X-Ray Photoelectron Spectrometer (XPS) (K-Alpha XPS, Thermo Fisher Scientific Inc., Waltham, MA, USA) was used to determine the atomic composition of the membrane active layer.

The CD of the PA film was calculated based on the O/N elemental ratio from the XPS spectra. The theoretical O/N ratio is 1.0 when the PA layer is fully cross-linked ($n = 1$), i.e., all the O and N atoms are associated with the amide groups to give a 1:1 ratio. This ratio becomes 2:1 for linear polyamide with no cross-linking ($n = 0$). To calculate the CD, the following equations was used [22]:

$$\frac{O}{N} = \frac{3m + 4n}{3m + 2n}, \text{and } m + n = 1, \tag{13}$$

where m and n are the crosslinked and linear portions, respectively. The CD is then obtained by $m \times 100\,\%$.

2.5. MD simulations

2.5.1. Atomistic models setup

To mimic the experimental IP procedures, a 15.0 nm-thick PA selective layer for each membrane was simulated via MD, with 1760 potential amine reaction sites and 1980 potential acid chloride reactions sites. These monomers were then placed in separate 3D-periodic cells, with a cross-section size of 5.0 × 5.0 nm. The PA layer was then synthesized by assembling the two cells perpendicular to the cross-sectional plane, representing the interface between amine and acid chloride monomer layers. The crosslinking reaction predominantly occurs at the interface between MPD and TMC [12], as illustrated in Fig. S12. This reaction is analyzed within the canonical ensemble (NVT), applying an initial cutoff distance of 4.5 Å to accurately simulate molecular interactions. Virtual elastic springs were introduced between amino nitrogen atoms and acyl carbon atoms for a specific cutoff distance. The crosslinked PA configuration underwent further optimization using the isothermal-isobaric ensemble (NPT) for a duration of 1 ns. The crosslinking reaction was then performed by gradually increasing the cutoff distance by 0.5 Å at each step until the desired CD was attained. The details about the crosslinking algorithms and molecular model generation was reported in previous studies [11,12].

2.5.2. NEMD simulations

NEMD simulations, shown in Fig. S13, were performed to study salt and water transport at low/high pressure within the PA membrane, with dimensions of 5.0 nm by 5.0 nm by 24.0 nm along the x, y, and z directions. Graphene pistons were positioned at z = 0.0 nm and z = 24.0 nm, respectively. The PA film located between z = 6.0 nm and z = 21.0 nm.

To describe the atomic interactions including graphene, water, and PA films, parameterized polymer consistent force field (PCFF) was applied [23–25]. Wherein, the Non-bonded interactions, Lennard-Jones (LJ) and Coulomb potentials, were:

$$U_{\text{non-bonded}} = C\frac{q_i q_j}{\varepsilon r_{ij}} + \varepsilon_{ij}\left[2\left(\frac{\sigma_{ij}}{r_{ij}}\right)^9 - 3\left(\frac{\sigma_{ij}}{r_{ij}}\right)^6\right] \tag{14}$$

where r_{ij} is the distance between the ith and jth atom, σ_{ij} represents the interatomic distance where two atoms show the minimum potential, ε_{ij} is the LJ potential' well depth, and q_i and q_j are respectively the ith and jth atom' charges. C defines a conversion factor, ε is the dielectric constant. The 6th-power combination rule:

$$\varepsilon_{ij} = \sqrt{\varepsilon_i \varepsilon_j}\left(2r_{ii}^3 r_{jj}^3\right) \Big/ \left(r_{ii}^6 + r_{jj}^6\right) \text{ and } \sigma_{ij} = \left(\sigma_{ii}^6 + \sigma_{jj}^6\right)^{\frac{1}{6}} \Big/ 2^{\frac{1}{6}} \tag{15}$$

was employed to describe the interatomic interactions. A particle-particle particle-mesh (PPPM) solver was utilized to account for long-range electrostatic interactions. A force tolerance of 10^{-4} was set to ensure the desired level of accuracy in the simulations. Additionally, a cutoff distance of 1.0 nm was employed to define the truncation of non-bonded interactions, thereby limiting the range over which these interactions were considered in the simulations.

The Large-scale Atomic/Molecular Massively Parallel Simulator (LAMMPS) package [26] was used to perform all MD simulations. The Velocity-Verlet algorithm was employed as the integration method to numerically solve the equations of motion for the atoms in system. A time step of 1.0 fs was set to advance the simulation forward in time. The simulation was initiated with energy minimization, following with 150-ns equilibrium molecular dynamics (EMD) simulations under the NVT ensemble. Subsequently, NEMD simulations were performed where a pressure difference (ΔP), 10, 20, 30, 60, 90, 120, or 150 MPa, was applied to the left piston, while the right piston is kept at a pressure of 0.1 MPa. The Nosé-Hoover thermostat [27,28] was adopted to maintain the system temperature at 300 K.

3. Results

3.1. Compaction and relaxation behavior of hand-cast RO membranes

XPS analysis confirms the C, N, and O elemental ratios in the PA coating films of all five membranes (Table S1). The PA layers exhibit a higher *CD* when prepared with a greater ratio of MPD, while increasing PPD content reduces the *CD*. In MD simulations, the *CD*s of the membranes were fixed to align with experimentally prepared membranes, in an attempt to ensure equivalent PA film mechanical properties in simulations and in experiments.

Wet-testing results are presented in Fig. 1, with additional data for representative commercial RO membranes in Fig. S1. Consistent with previous work [4], the commercial RO membrane shows both irreversible and reversible compaction during wet testing. Notably, water permeance declines with increasing applied pressure and a small amount of permeance is recovered via relaxation, although irreversible compaction is dominant in this case. Relaxation time has a minimal impact on the relaxation ratio (*RR*). Specifically, a 24-h relaxation period results in an RR that is 4 % higher than that observed after just 30 min. This suggests that the majority of the relaxation process occurs rapidly, although some minor reversible compaction may require additional time to resolve. *CD*s of the PA coating films decrease in the order of M1 (87 %) > M2 (77 %) > M3 (69 %) > M4 (60 %) ≫ M5 (31 %). Correspondingly, the initial

water permeances (*A*₀) of the high *CD* membranes, M1 (2.28 LMH/bar), M2 (1.46 LMH/bar), and M3 (0.91 LMH/bar), are lower than the low *CD* counterparts, M4 (5.12 LMH/bar) and M5 (16.7 LMH/bar) (Fig. 1A–E). The enhanced water permeances observed in membranes M1 and M2 compared to M3 can be attributed to the utilization of triethylamine (TEA) and camphorsulfonic acid (CSA), as well as differences in the solvents [29]. High *CD* membranes (M1-M3) also show a lower compaction impact—26%–36 % permeance loss—compared to low *CD* membranes (M4-M5) which exhibit 88%–91 % loss after 60 min (Fig. 1F and Fig. S2). The membrane M1, with highest *CD*, experienced 65 % less compaction than the M5, which has lowest *CD*. Further, high *CD* membranes exhibit superior relaxation ratio to the low *CD* ones: M1 (21.05 %) > M2 (20.37 %) > M3 (19.55 %) > M4 (18.89 %) ≫ M5 (3.83 %). M1 exhibited a 17.2 % higher relaxation ratio compared to M5. Regardless of *CD*, all membranes compact within 5 min, reaching relative stability within 30 min at an applied pressure of 60 bar. The wet-testing data confirms that PA films with higher *CD* experience less compaction and greater recovery via relaxation compared to PA films with lower *CD*. Commercial SWRO are reported to show higher *CD* than BWRO does in general [30], which explains the similar behaviors observed in the commercial membrane testing where BWRO experiences more compaction and less relaxation in contrast to SWRO.

The molecular weight cutoffs (MWCO) of M1 to M5 were determined to provide additional insights into the pore structure and crosslinking
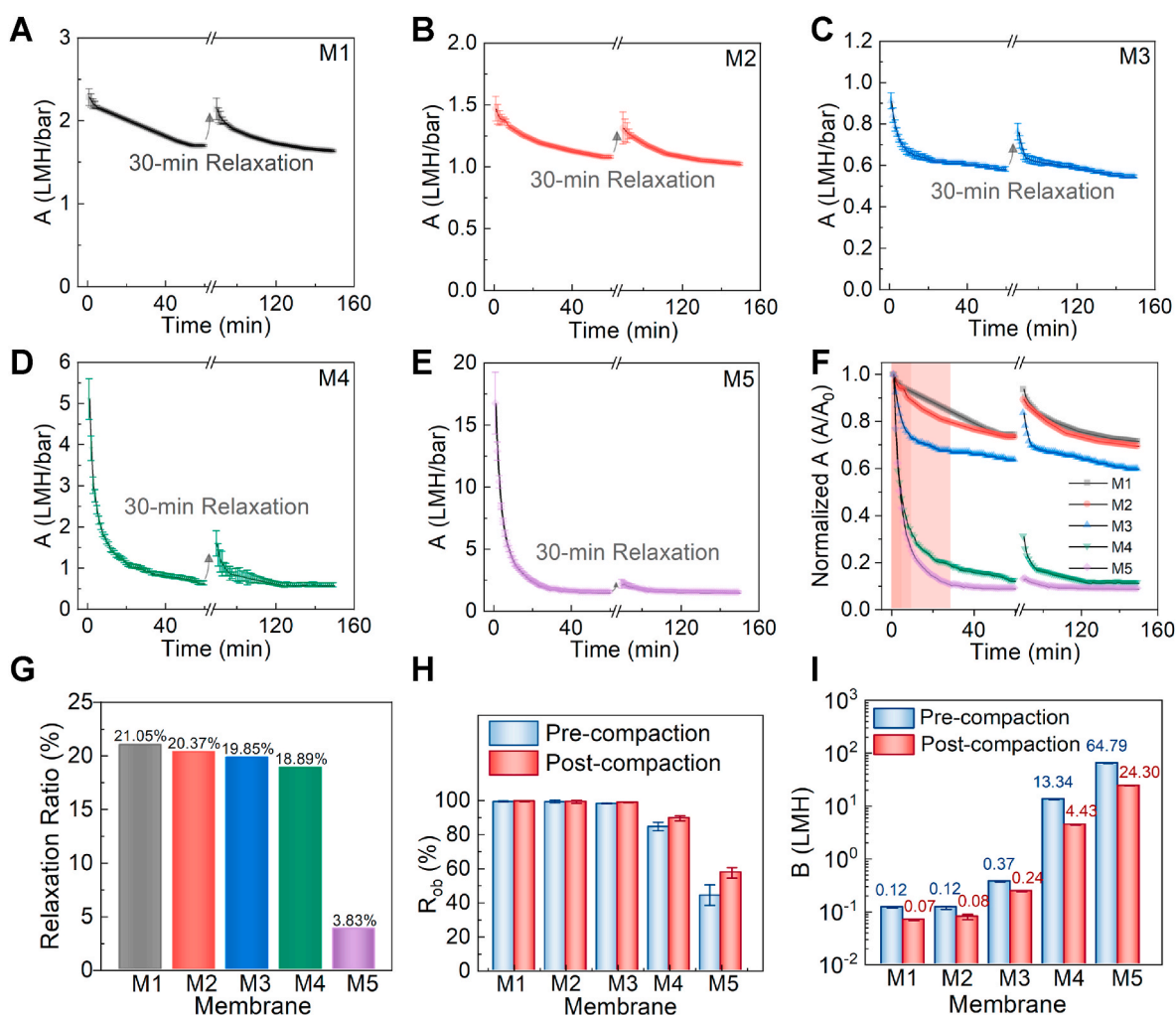
Fig. 1. Membrane wet-testing performance. (A) M1, (B) M2, (C) M3, (D) M4, (E) M5 water permeance as a function of time. (F) normalized water permeance of M1 to M5. (G) relaxation ratio of M1 to M5. (H) observed rejection of M1 to M5 before and after compaction. (I) solute (NaCl) permeability of M1 to M5 before and after compaction. All experiments are conducted at 60 bar, 20°C. In salt rejection testing, 32 g/L NaCl feed solution is used. Water permeance is presented in LMH/bar (liter m⁻² h⁻¹ bar⁻¹). Solute permeability is presented in LMH (liter m⁻² h⁻¹).

degree of the membranes. This was accomplished by assessing their rejection of polyethylene glycol (PEG) as a function of the PEG molecular weight, as illustrated in Fig. S3. The MWCO results confirmed that M1 (96 Da), M2 (102 Da), and M3 (114 Da) exhibited a tighter pore structure compared to M4 (298 Da) and M5 (496 Da). Salt rejection data provide further insights into how compaction influences membrane selectivity, depicted in Fig. 1H. Regardless the *CD* of the PA layer, all tested membranes demonstrated enhanced rejection (32,000 ppm NaCl at 60 bar) after 60-min compaction (and 30-min relaxation): M1 (99.15 %–99.51 %), M2 (99.06 %–99.29 %), M3 (98.00 %–98.84 %), M4 (84.39 %–89.69 %), and M5 (44.00 %–57.69 %). This upswing in rejection is consistent with the decrease in water permeability, and

indicates compaction is densifying ("tightening") the pore structure, which subsequently restricts both solvent and solute transport. Fig. 1I further corroborates this finding with the decline in solute permeability *B* post-compaction: M1 (0.12 LMH to 0.07 LMH), M2 (0.12 LMH to 0.08 LMH), M3 (0.37 LMH to 0.24 LMH), M4 (13.34 LMH to 4.43 LMH), and M5 (64.79 LMH to 24.30 LMH). The NaCl rejection trend: M1 (99.51 % ± 0.10 %) > M2 (99.29 % ± 0.09 %) > M3 (98.84 % ± 0.18 %) > M4 (89.69 % ± 1.51 %) ≫ M5 (57.69 % ± 3.04 %) (Fig. 1H) follows the MWCO results. These direct relationship between *CD* and *A* and *B* values highlight the impact of the PA selective layer *CD* properties on membrane performance.
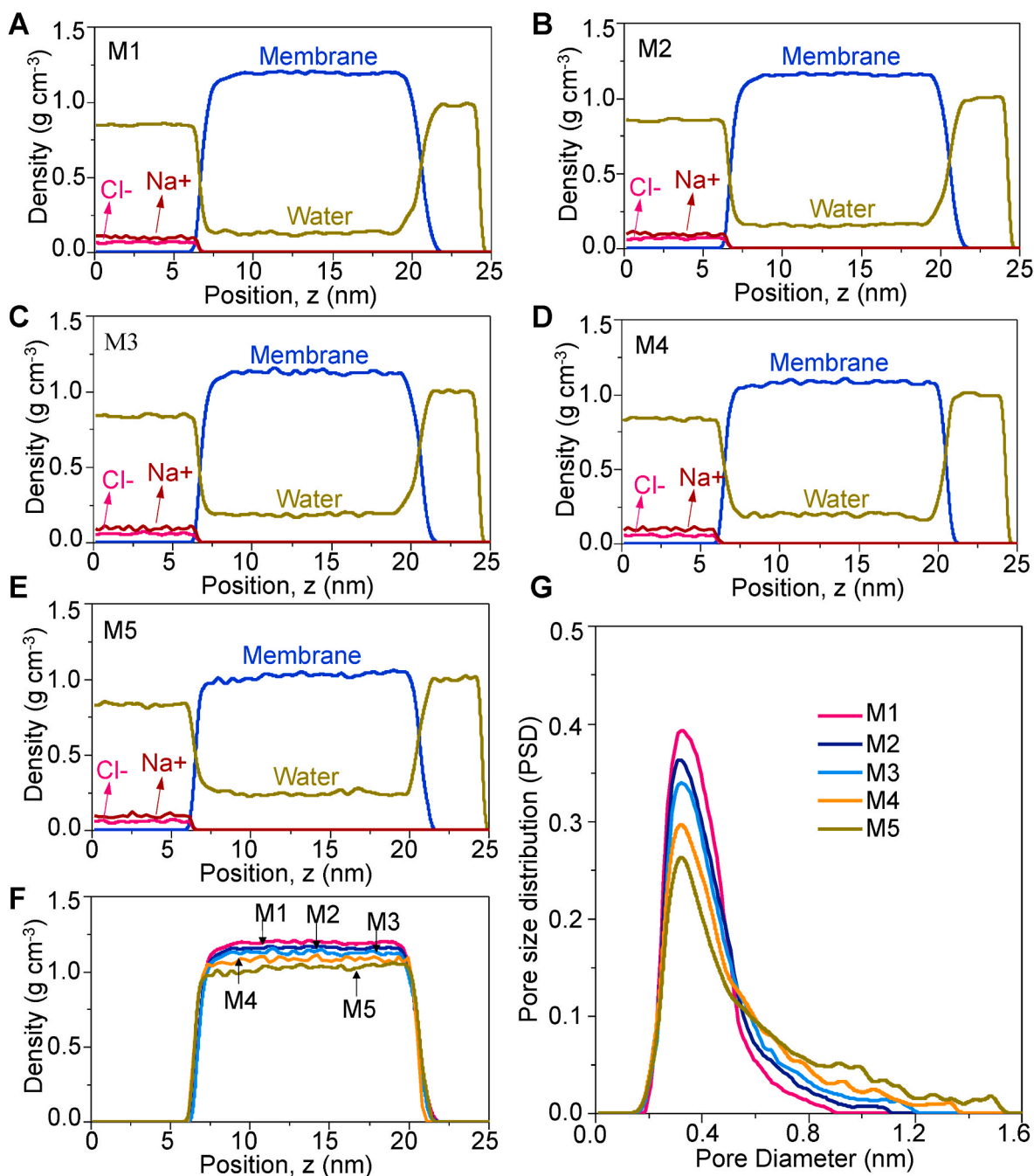

Fig. 2. Axial local density profiles of components for five hydrated PA membrane systems including (A) M1, (B) M2, (C) M3, (D) M4, and (E) M5. The blue, light green, wine, and light red represent the component of PA membrane, water, chloride (Cl⁻), and sodium ions (Na⁺) within five systems, respectively. (F) comparison of the axial local density profiles along z direction. (G) pore size distribution (PSD) of M1, M2, M3, M4, and M5. (For interpretation of the references to colour in this figure legend, the reader is referred to the Web version of this article.)

3.2. MD simulations of water transport and PA film

The MD-derived local density profiles of PA selective layers are shown in Fig. 2. During the simulation period, no chloride (Cl^-) or sodium ions (Na^+) crossed the PA layers, as confirmed in Fig. S4, yielding 100 % ion rejection in our simulations. However, water transport through these films is clearly observed. Comparisons in Fig. 2F suggest that PA film density follows the sequence M1 > M2 > M3 > M4 > M5,

closely mirroring *CD* results derived from XPS analysis (Table S1). As depicted in Fig. 2G, and also shown in Table S4, the PSD exhibits a higher proportion of sub-0.5 nm pores in M1-M3, whereas M4 and M5 display an increasing fraction of pores with diameter >0.5 nm, with M5 showing the most. These observations align with the conclusion that M1-M3 possess "tighter" structures, whereas M4 exhibits a structure that is "looser" than M1-M3, but "tighter" than M5, as evident by the MWCO testing results (Fig. S3). The density and PSD data of PA films
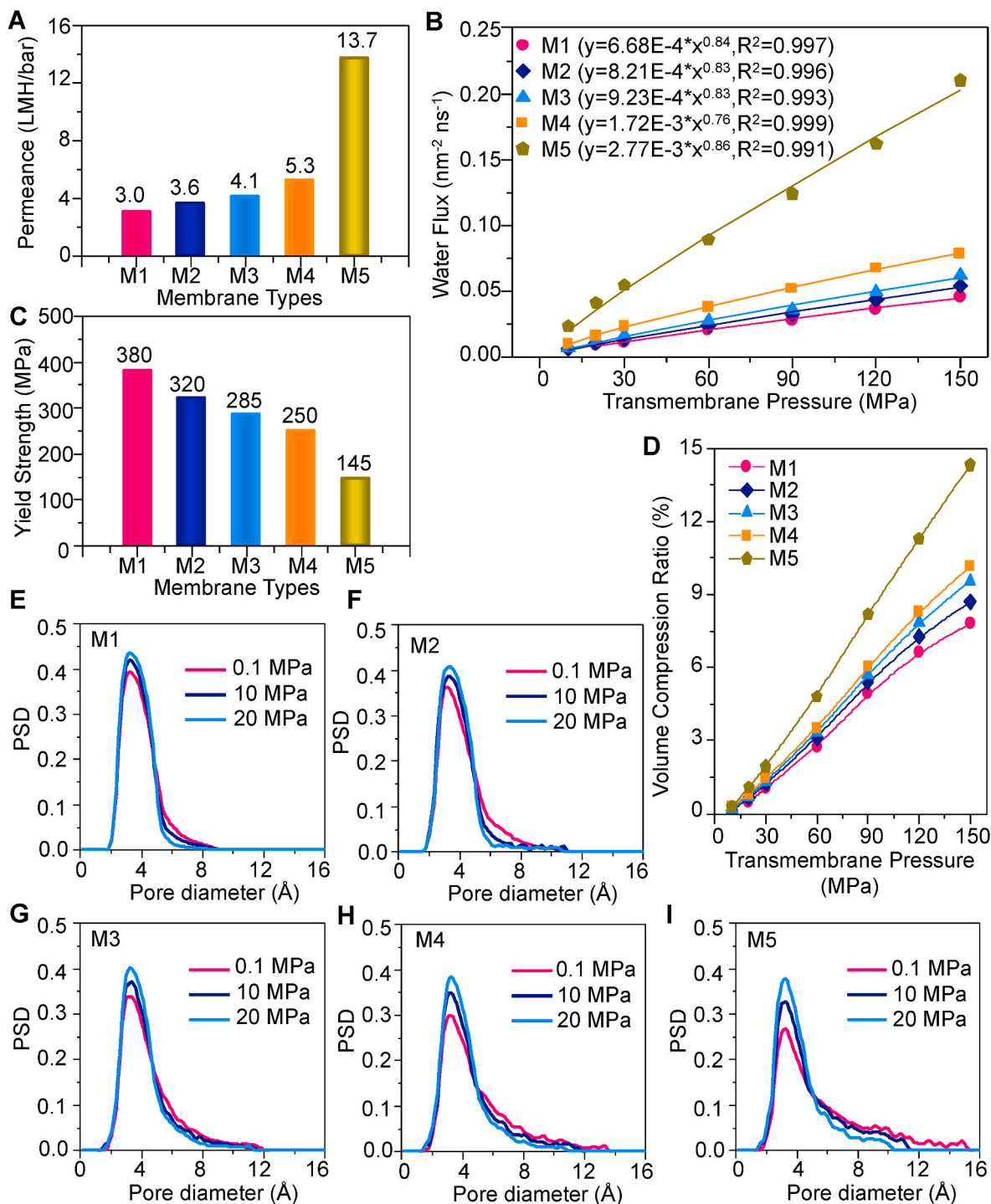
Fig. 3. Water transport and mechanical properties of simulated PA films. (A) calculated water permeance of five types of PA film simulated. (B) Number water flux of five types of PA layers as a function of transmembrane pressure, with power regression fitted with $R^2 > 0.99$. (C) Compressive yield strengths of simulated PA layers, extracted from stress-strain curve (Fig. S8). (D) Volume compression ratio of membrane as a function of pressures. (E) Pore size distribution (PSD) in respond to three pressures including 0.1 MPa, 10 MPa, and 20 MPa for five PA layers including (E) M1, (F) M2, (G) M3, (H) M4, and (I) M5.

corroborate the water and solute permeability results observed in wet-testing. As the PA selective layer becomes "tighter," both water and solute permeability decrease while the observed salt rejection increases.

The water permeance results from MD simulations corroborate wet-testing data. Using a linear regression, shown in Fig. S5, the water permeances for all five simulated PA layers are presented in Fig. 3A. Accounting for membrane thickness (Fig. S6), the intrinsic water permeability (permeance times membrane thickness) values are consistent between wet-testing (Fig. 1) and MD simulations (Fig. 3A). Specifically, experimental and simulated water permeability are respectively 73 and 45 nm·LMH/bar for M1, 68 and 54 nm·LMH/bar for M2, 66 and 61 nm·LMH/bar for M3, 78 and 79 nm·LMH/bar for M4, and 241 and 206 nm·LMH/bar for M5. The use of triethylamine (TEA) and camphorsulfonic acid (CSA) in M1 and M2 enhances PA membrane permeablity by making a denser, but thinner film and the use of hexane makes a thinner, denser PA layer than Isopar-G when all other factors are held constant [31]. That said, in NEMD simulations, all the films are the same thickness; hence, the permeability is strictly determined by the extent of crosslinking, which governs the microporosity of the PA layer. With increasing applied pressure from 10 MPa to 150 MPa, all five PA layers produce higher water flux, as presented in Fig. S7. As pressure increases (Fig. 3B), water flux increases non-linearly for all five PA layer types, as illustrated by the power-law regression, suggesting compaction of the PA films. The alignment of water permeability and compaction behavior in both experiments and simulations gives confidence to the validity of the simulations, which provide much greater insight into the characteristics of PA films at the nanoscale.

The stress-strain (Fig. S8) and the compressive yield strength data (Fig. 3C) for simulated PA layers indicate greater mechanical stability for M1-M3 over M4 and M4 over M5. The volume compression ratio (Fig. 3D) for the five simulated PA layers follows the trend M1 < M2 < M3 < M4 < M5, which follows PA film *CD*. This finding underscores the importance of a high *CD* to enhance the PA film mechanical strength, as shown previously [11]. Pore size distribution (PSD) at pressures of 0.1 (atmospheric pressure), 10, and 20 MPa are shown in Fig. 3E–G and Table S4. The atmospheric pressure PSDs are the same as discussed in Fig. 2, skewing larger from M1-M3 to M4 to M5, where M1-M3 has ~10 % more sub-0.5 nm pores than M4 and ~14 % more sub-0.5 nm pores than M5. Upon increasing pressure from 0.1 MPa to 20 MPa, all simulated PA layers exhibit a similar response: the proportion of sub-0.5 nm diameter pore increase, while supra-0.5 nm diameter pores decrease. This is evidence of PA layer compaction and densification.

3.3. PA compaction and relaxation

Videos of MD-simulated PA films compacting under pressure are provided (Figs. S9–11) to further illustrate the rate and extent of PA layer compaction and relaxation. Snapshots of hydrated PA film following compaction and relaxation at 150 ns and 300 ns simulation time are provided, accompanied by porosity data (free volume over total volume) for each stage (Fig. 4). At ambient pressure, M1 is least porous (0.237), M2 (0.247) slightly more so, followed by M3 (0.267), and M4 (0.275). M5 is the most porous (0.312). As shown in Fig. 4, at 150 MPa pressure, all PA layers experience compaction (red lines), with M1-M3 experiencing the least, M4 more, and M5 the most. This compaction corresponds to a decrease in PA film porosity. Upon relieving the applied pressure, the PA films (yellow lines) relax and recover *nearly* 100 % of their original porosity, demonstrating the reversible nature of compaction (or relaxation) observed in our wet-testing experiments. This supports the observation of reduced water permeance under load (compaction), and recovery of water permeance after pressure relief (relaxation). At lower pressures, the compaction and relaxation effects simulated are subtler, yet they still reflect the behavior observed in the polyamide films subjected to higher pressures, as illustrated in Fig. S14. In line with all the results discussed above, membranes with higher *CD* are less susceptible to compaction and exhibit higher relaxation ratio

when exposed to the same applied pressure compared to lower *CD* counterparts. The relaxation behavior observed in this study aligns with previous findings by Davenport et al. [7], where no significant changes in polyamide selective layer thickness or roughness were detected in commercial RO membranes after high-pressure testing. These findings suggest that the observed stability in physical characteristics can be attributed to the strong relaxation properties of the polyamide layer, which effectively returns to its original state post-deformation.

The PA selective layer of composite RO membranes exhibits (largely reversible) compaction under high applied pressure. The extent of compaction varies based on the mechanical properties of the selective layer, which appear to be largely driven by the *CD*. Moreover, the microporoisity of the PA layers affects water permeance by determining the permeation path length of the solvent [32]. M1-M3 show a crumbled structure with a longer path length and a high *CD* (tight pore structure), resulting in low permeance. In contrast, M4 has a flatter microporosity with a shorter path length and a low *CD* (loose pore structure), leading to higher permeance. However, despite these differences, M5 experiences more compaction than M1-M3, indicating the dominant role of crosslinked pore structure in compaction of membranes.

Relaxation of the crosslinked (thermoset) PA layer occurs once the applied pressure is withdrawn, a consequence of its inherent elastic properties. In the realm of gas separation membranes, higher *CD* usually results in more significant and quicker relaxation behaviors. This aligns with our observation of rapid relaxation in both commercial and hand-cast RO membranes, attributable to the highly crosslinked PA film with limited molecular mobility [33,34]. Additionally, the PA layer intricate mircrostructure, low porosity, and small pore size confer exceptional mechanical strength (Fig. 3C and Fig. S8), making it both resistant to pressure and quick to relax upon unloading.

However, the relaxation is not completely reversible, suggesting that the PA layers undergo minor microstructural changes induced by compaction, akin to physical aging in gas separation membranes [34]. Such behavior can lead to permanent alterations in membrane properties through creep and partial recovery. Enhancing membrane resistance to compaction (in water applications) or aging (in gas separation) hinges on increasing *CD*, but a theoretical 100 % *CD* is difficult to attain due to the self-inhibiting nature of interfacial polymerization (IP) [35–37]. This limitation arises as early-stage PA film obstructs the diffusion of unreacted monomers. Nevertheless, *CD* can be effectively tailored through various IP parameters like monomer mole ratio, reaction time, temperature, and additives etc. [12,35,38,39].

The physical phenomena of compaction and relaxation explain the experimentally observed permeation behavior observed during wet testing. These findings constitute a significant step forward in understanding the functional behavior of RO membranes, emphasizing the crucial role of the PA layer structural and mechanical characteristics in determining filtration performance.

4. Conclusion and implications

By integrating wet-testing experiments with SEM images, XPS analysis, and MD simulations, we have elucidated the mechanical properties, mechanisms of compaction, and evidence for relaxation in PA coating films of composite RO membranes. Composite RO membranes with a higher *CD* in the PA film exhibit higher salt rejection, undergo less compaction, and recover to a greater extent via relaxation. MD simulations reproduce experimental observations and elucidate the mechanisms underlying this behavior. Specifically, higher *CD* endows the film with greater mechanical strength along with a tighter pore structure, and thus, the membrane experiences less compaction and more complete relaxation relative to PA films with a lower *CD*. Relaxation occurs within minutes in experiments and within 100's of nanoseconds in simulations; experimentally, no significant changes in relaxation occur beyond 30 min for up to 24 h. The relaxation (reversible compaction) of the composite membrane is attributed to the thermoset property of the
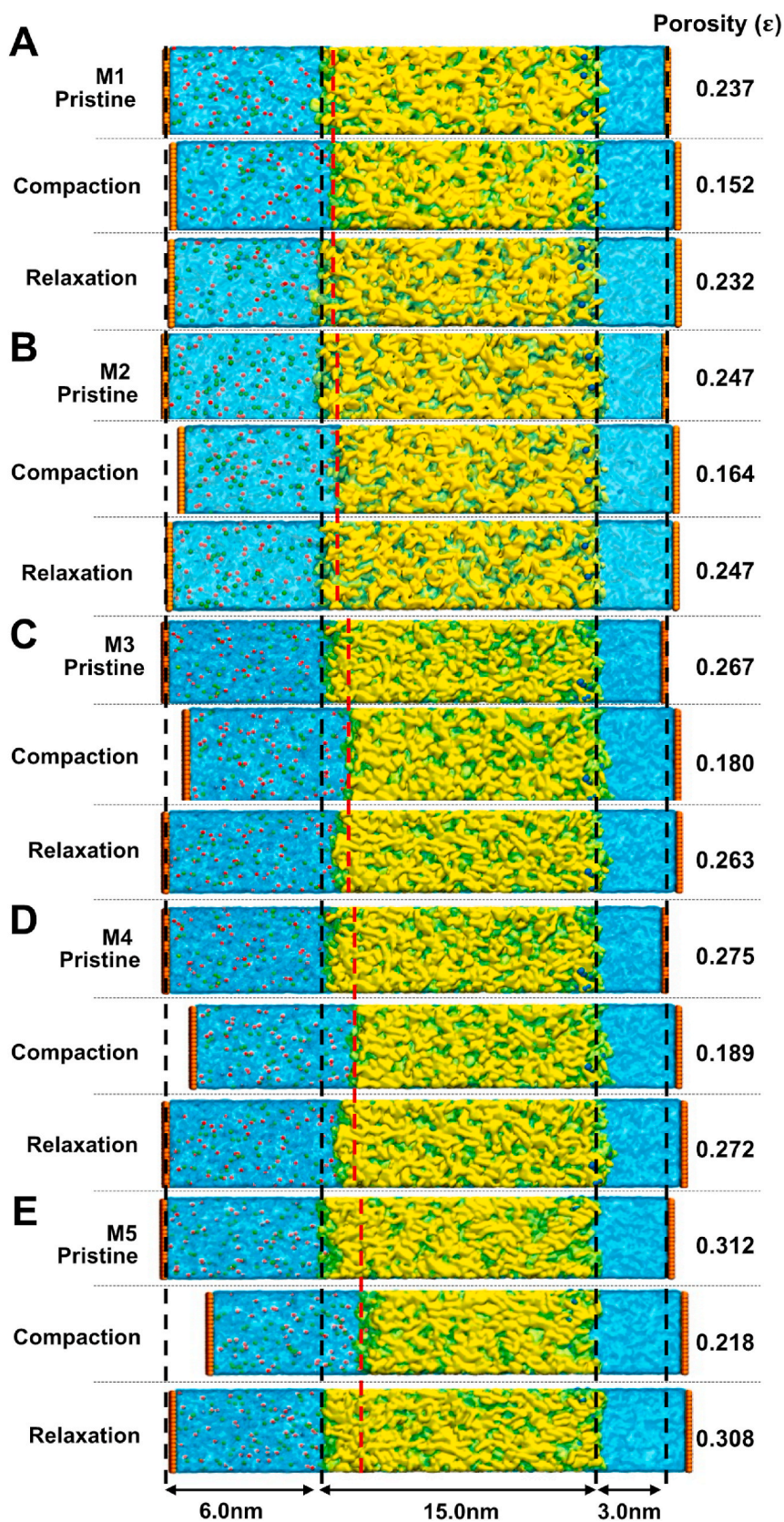
Fig. 4. PA film compaction and relaxation in NEMD. (A) M1; (B) M2, (C) M3, (D) M4, and (E) M5 compaction, relaxation, and porosity under 150 MPa applied pressure at different stages. The compaction image is obtained at 150 ns simulation time with the applied pressure loaded on the feed. Then the pressure is released for another 150 ns simulation time, and the relaxation image is captured afterwards, at 300 ns simulation time.

PA active layer whereas the irreversible compaction is due to the densification of the PSU porous support skin layer (underneath PA layer) of the polysulfone support [4,40].

This comprehensive study on compaction and relaxation of composite PA membranes provides new insights with implications for the development of new compaction-resistant composite RO membranes – even at pressures exceeding the current state of the art limit of 120 bar. A PA film with very high *CD* is required to minimize permeability decline by compaction and complete recovery by relaxation in addition to high salt rejection. Observations of relaxation provide insights into industrial RO operations. Following post cleaning, RO facilities often see substantial, but not complete recovery of initial water permeance attributed to incomplete removal of fouling and scaling materials from the membrane. However, this unrecoverable fouling may often be due to irreversible compaction. This was previously shown to be the case in a low-pressure RO application of municipal wastewater recycling [41].

Evidence of PA film porosity and permeability changes (occurring in tandem) due to compaction and relaxation may have further implications for understanding the fundamental mechanisms governing water transport RO membranes. From the combined experimental and MD simulation results in this study, we observe (i) the films possess a microporous structure with pores ranging from 0.4 to 0.5 nm and ambient porosity ranging from about 24 % to 31 %, but reduced to 15 % to 20 % under pressure, (ii) there is no water concentration gradient across the film, and (iii) the PA layer compacts and relaxes with pressure application and release. Hence, the results support pressure-driven viscous flow, with compaction induced by the combined effects of applied pressure and flow through the membrane [42,43]. This offers further support for the same observations derived from NEMD simulations in another recent study [14], where it was reported that water transports in clusters through interconnected free volume elements (or pores) in PA films. Our new observations confirm PA films experience compaction, which may be interpreted as (partial or complete) collapse of (some or all of) the interconnected free volume elements within the crosslinked films.

Funding

CRediT authorship contribution statement

Jishan Wu: Writing – review & editing, Writing – original draft, Visualization, Validation, Methodology, Investigation, Formal analysis, Data curation, Conceptualization. **Jinlong He:** Writing – original draft, Visualization, Validation, Software, Formal analysis, Data curation, Conceptualization. **Javier A. Quezada-Renteria:** Writing – review & editing. **Jason Le:** Validation, Investigation. **Kay Au:** Validation, Data curation. **Kevin Guo:** Validation, Data curation. **Minhao Xiao:** Methodology, Investigation. **Xinyi Wang:** Methodology. **Derrick Dlamini:** Investigation. **Hanqing Fan:** Investigation. **Kevin Pataroque:** Methodology. **Yara Suleiman:** Data curation. **Sina Shahbazmohamadi:** Investigation. **Menachem Elimelech:** Supervision. **Ying Li:** Supervision, Funding acquisition, Conceptualization. **Eric M.V. Hoek:** Writing – review & editing, Supervision, Funding acquisition, Conceptualization.

Declaration of competing interest

All authors declare that there are no financial and personal relationships with other individuals or organizations that can inappropriately influence this work; there is no professional or other personal interest of any nature or kind in any product, service or company that could be construed as influencing the position presented in, or the review of, this manuscript.

Data availability

Data will be made available on request.

Appendix A. Supplementary data

Supplementary data to this article can be found online at https://doi.org/10.1016/j.memsci.2024.122893.

References

[1] A. Edalat, E. Hoek, Techno-economic analysis of RO desalination of produced water for beneficial reuse in California, Water 12 (7) (2020) 1850.

[2] E.M.V. Hoek, D. Jassby, R.B. Kaner, J. Wu, J. Wang, Y. Liu, U. Rao, Sustainable Desalination and Water Reuse, Morgan & Claypool Publishers, 2021.

[3] M. Elimelech, W.A. Phillip, The future of seawater desalination: energy, technology, and the environment, science 333 (6043) (2011) 712–717.

[4] J. Wu, B. Jung, A. Anvari, S. Im, M. Anderson, X. Zheng, D. Jassby, R.B. Kaner, D. Dlamini, A. Edalat, E.M.V. Hoek, Reverse osmosis membrane compaction and embossing at ultra-high pressure operation, Desalination 537 (2022) 115875, https://doi.org/10.1016/j.desal.2022.115875.

[5] J.R. McCutcheon, M.S. Mauter, Fixing the desalination membrane pipeline, Science 380 (6642) (2023) 242–244.

[6] M.T.M. Pendergast, J.M. Nygaard, A.K. Ghosh, E.M.V. Hoek, Using nanocomposite materials technology to understand and control reverse osmosis membrane compaction, Desalination 261 (3) (2010) 255–263.

[7] D.M. Davenport, C.L. Ritt, R. Verbeke, M. Dickmann, W. Egger, I.F.J. Vankelecom, M. Elimelech, Thin film composite membrane compaction in high-pressure reverse osmosis, J. Membr. Sci. 610 (2020) 118268.

[8] K.H. Chu, J.S. Mang, J. Lim, S. Hong, M.-H. Hwang, Variation of free volume and thickness by high pressure applied on thin film composite reverse osmosis membrane, Desalination 520 (2021) 115365.

[9] R.A. Peterson, A.R. Greenberg, L.J. Bond, W.B. Krantz, Use of ultrasonic TDR for real-time noninvasive measurement of compressive strain during membrane compaction, Desalination 116 (2–3) (1998) 115–122.

[10] M. Ding, A. Ghoufi, A. Szymczyk, Molecular simulations of polyamide reverse osmosis membranes, Desalination 343 (2014) 48–53.

[11] J. He, J. Yang, J.R. McCutcheon, Y. Li, Molecular insights into the structure-property relationships of 3D printed polyamide reverse-osmosis membrane for desalination, J. Membr. Sci. 658 (2022) 120731.

[12] J. He, J.R. McCutcheon, Y. Li, Effect of different manufacturing methods on polyamide reverse-osmosis membranes for desalination: insights from molecular dynamics simulations, Desalination 547 (2023) 116204.

[13] J. He, T. Arbaugh, D. Nguyen, W. Xian, E.M.V. Hoek, J.R. McCutcheon, Y. Li, Molecular mechanisms of thickness-dependent water desalination in polyamide reverse-osmosis membranes, J. Membr. Sci. 674 (2023) 121498.

[14] L. Wang, J. He, M. Heiranian, H. Fan, L. Song, Y. Li, M. Elimelech, Water transport in reverse osmosis membranes is governed by pore flow, not a solution-diffusion mechanism, Sci. Adv. 9 (15) (2023) eadf8488.

[15] H.K. Lonsdale, U. Merten, R.L. Riley, Transport properties of cellulose acetate osmotic membranes, J. Appl. Polym. Sci. 9 (4) (1965) 1341–1362.

[16] M. Mulder, J. Mulder, Basic Principles of Membrane Technology, Springer Science & Business, 1996. Media.

[17] X. Jin, A. Jawor, S. Kim, E.M.V. Hoek, Effects of feed water temperature on separation performance and organic fouling of brackish water RO membranes, Desalination 239 (1–3) (2009) 346–359.

[18] J. Wang, D.S. Dlamini, A.K. Mishra, M.T.M. Pendergast, M.C.Y. Wong, B.B. Mamba, V. Freger, A.R.D. Verliefde, E.M.V. Hoek, A critical review of transport through osmotic membranes, J. Membr. Sci. 454 (2014) 516–537.

[19] E.M.V. Hoek, A.S. Kim, M. Elimelech, Influence of crossflow membrane filter geometry and shear rate on colloidal fouling in reverse osmosis and nanofiltration separations, Environ. Eng. Sci. 19 (6) (2002) 357–372.

[20] J. Wang, Y. Mo, S. Mahendra, E.M.V. Hoek, Effects of water chemistry on structure and performance of polyamide composite membranes, J. Membr. Sci. 452 (2014) 415–425.

[21] Wu, J.; Xiao, M.; Quezada-Renteria, J.A.; Hou, Z.; Hoek, E., Sample preparation matters: scanning electron microscopic characterization of polymeric membranes. J. Membr. Sci. Lett. 4 (1) 100073.

[22] S.H. Kim, S.-Y. Kwak, T. Suzuki, Positron annihilation spectroscopic evidence to demonstrate the flux-enhancement mechanism in morphology-controlled thin-film-composite (TFC) membrane, Environ. Sci. Technol. 39 (6) (2005) 1764–1770.

[23] H. Sun, S.J. Mumby, J.R. Maple, A.T. Hagler, An ab initio CFF93 all-atom force field for polycarbonates, J. Am. Chem. Soc. 116 (7) (1994) 2978–2987, https://doi.org/10.1021/ja00086a030.

[24] H. Sun, Ab initio calculations and force field development for computer simulation of polysilanes, Macromolecules 28 (3) (1995) 701–712, https://doi.org/10.1021/ma00107a006.

[25] H. Heinz, T.-J. Lin, R. Kishore Mishra, F.S. Emami, Thermodynamically consistent force fields for the assembly of inorganic, organic, and biological nanostructures: the INTERFACE force field, Langmuir 29 (6) (2013) 1754–1765, https://doi.org/10.1021/la3038846.

[26] S. Plimpton, Fast Parallel algorithms for short-range molecular dynamics, J. Comput. Phys. 117 (1) (1995) 1–19, https://doi.org/10.1006/jcph.1995.1039.

[27] S. Nosé, A unified formulation of the constant temperature molecular dynamics methods, J. Chem. Phys. 81 (1) (1984) 511–519, https://doi.org/10.1063/1.447334.

[28] W.G. Hoover, Canonical dynamics: equilibrium phase-space distributions, Phys. Rev. 31 (3) (1985) 1695–1697, https://doi.org/10.1103/PhysRevA.31.1695.

[29] A.K. Ghosh, B.-H. Jeong, X. Huang, E.M. Hoek, Impacts of reaction and curing conditions on polyamide composite reverse osmosis membrane properties, J. Membr. Sci. 311 (1–2) (2008) 34–45.

[30] C.Y. Tang, Y.-N. Kwon, J.O. Leckie, Effect of membrane chemistry and coating layer on physiochemical properties of thin film composite polyamide RO and NF membranes: I. FTIR and XPS characterization of polyamide and coating layer chemistry, Desalination 242 (1–3) (2009) 149–167.

[31] A.K. Ghosh, E.M. Hoek, Impacts of support membrane structure and chemistry on polyamide–polysulfone interfacial composite membranes, J. Membr. Sci. 336 (1–2) (2009) 140–148.

[32] H. An, J.W. Smith, B. Ji, S. Cotty, S. Zhou, L. Yao, F.C. Kalutantirige, W. Chen, Z. Ou, X. Su, Mechanism and performance relevance of nanomorphogenesis in polyamide films revealed by quantitative 3D imaging and machine learning, Sci. Adv. 8 (8) (2022) eabk1888.

[33] C.H. Lau, X. Mulet, K. Konstas, C.M. Doherty, M.-A. Sani, F. Separovic, M.R. Hill, C. D. Wood, Hypercrosslinked additives for ageless gas-separation membranes, Angew. Chem., Int. Ed. 55 (6) (2016) 1998–2001, https://doi.org/10.1002/anie.201508070.

[34] A.J. Hill, S.J. Pas, T.J. Bastow, M.I. Burgar, K. Nagai, L.G. Toy, B.D. Freeman, Influence of methanol conditioning and physical aging on carbon spin-lattice relaxation times of poly (1-trimethylsilyl-1-propyne), J. Membr. Sci. 243 (1–2) (2004) 37–44.

[35] X. Lu, M. Elimelech, Fabrication of desalination membranes by interfacial polymerization: history, current efforts, and future directions, Chem. Soc. Rev. 50 (11) (2021) 6290–6307.

[36] H. Zhang, M.S. Wu, K. Zhou, A.W.-K. Law, Molecular insights into the composition–structure–property relationships of polyamide thin films for reverse osmosis desalination, Environ. Sci. Technol. 53 (11) (2019) 6374–6382.

[37] N. Li, M. Li, S. Lin, S. Cui, X. Zhang, Stoichiometric effect on the structural transformation and spatial variation of polyamide reverse osmosis membranes: a molecular dynamics study, J. Membr. Sci. (2023) 121980.

[38] B.J. Feinberg, E.M. Hoek, Interfacial Polymerization, Encyclopedia of Membrane Science and Technology, 2013, pp. 1–15.

[39] Y.J. Lim, K. Goh, M. Kurihara, R. Wang, Seawater desalination by reverse osmosis: current development and future challenges in membrane fabrication–A review, J. Membr. Sci. 629 (2021) 119292.

[40] C. Xu, Z. Wang, Y. Hu, Y. Chen, Thin-film composite membrane compaction: exploring the interplay among support compressive modulus, structural characteristics, and overall transport efficiency, Environ. Sci. Technol. (2024) 58, 19–8596.

[41] E.M. Hoek, J. Allred, T. Knoell, B.-H. Jeong, Modeling the effects of fouling on full-scale reverse osmosis processes, J. Membr. Sci. 314 (1–2) (2008) 33–49.

[42] M. Heiranian, H. Fan, L. Wang, X. Lu, M. Elimelech, Mechanisms and models for water transport in reverse osmosis membranes: history, critical assessment, and recent developments, Chem. Soc. Rev. (2023) 52. 8455-8480.

[43] H. Fan, P. Biesheuvel, M. Elimelech, Theory of expansion and compression of polymeric materials: Implications for membrane solvent flow under compaction, (2024)122576.